Particle and liquid motion in semi-solid aluminium alloys: a quantitative in situ micro-radioscopy study

S. Zabler[1*], A. Ershov[2], A. Rack[3], F. Garcia-Moreno[4], T. Baumbach[2], J. Banhart[4,5]

[1]Universität Würzburg, Institute of Physics and Astronomy, Würzburg Germany, *corresponding author, simon.zabler@physik.uni-wuerzburg.de, phone: [+49] (0)931-31 86261, fax: [+49] (0)931-31 81909.

[2]Karlsruher Institute of Technology, ANKA, Karlsruhe Germany, tilo.baumbach@kit.edu, ershov.alexey@gmail.com.

[3]European Synchrotron Radiation Facility, Grenoble France, alexander.rack@esrf.fr.

[4]Helmholtz Center Berlin – Functional Materials, Berlin Germany, garcia-moreno@helmholtz-berlin.de.

[5]Technische Universität Berlin, Berlin Germany, john.banhart@tu-berlin.de.

Abstract

Semi-solid melt exhibits a very unpredictable rheology and filling dynamics, when it is injected into thin-walled components. Optimization of the process requires visual insight into the casting process during the injection. For this purpose we inject semi-solid Al-Ge alloy into two different thin channel geometries while recording high-resolution radiographs at fast frame rates (up to 1000 images/s). The comparison of a bottleneck channel, which had been previously used for slower experiments, with a right-angle turn geometry reveals a significant influence of the channel's shape on the flow behavior of the particle-liquid mixture. While the bottleneck is quickly sealed with densified solid, turbulences in the right-angle turn apparently permit the solid particles and clusters to move conjointly with the liquid and thus achieve a more complete filling. Single particle trajectories and rapid break-up of solid skeletons in such a system are observed for the first time in situ.

Keywords: Semi-solid, X-ray radiography, synchrotron radiation, rheology, in-situ.

1. Introduction

Semi-solid metals are two-phase solid-liquid mixtures of unusual rheological properties [1]. While they are inert, they behave like elastic solids, whereas shearing causes a transition into a viscous mixture which can flow. Thus, they show shear thinning behaviour, i.e. the apparent viscosity drops exponentially when the shear rate is increased. The transition from a sponge-like locked solid phase filled by liquid to a viscous medium is marked by the breakup of the (percolated) solid skeleton into particles and/or clusters which can move individually through the liquid. This breakup is commonly referred to as the '*thixotropic effect*' [2]. Typical

alloys which are used for thixo- or rheocast components are aluminium and magnesium casting alloys (e.g. A356 or AZ91). Compared to high pressure die casting, semi-solid casting (SSC) processes operate at lower temperature which is associated with a number of advantages [3], namely that volume shrinkage effects are less pronounced, there is far less risk of hot cracking and void formation and die wear is reduced due to the low temperatures. The compositional range of casting alloys can be extended to larger melting intervals. On the other side, various difficulties lead to higher costs and have so far prevented the technology from becoming wide spread.

While the flow of the liquid phase can be described as a Newtonian fluid, little is known about the flow and rheology of a solid-liquid mixture [4]. The size and shape of solid particles / clusters, their motion, their ability and tendency to break up and regroup into different morphologies are a critical input required to model the filling dynamics of semi-solid injections [5]. There are many possible interactions: particle-particle as well as particle-liquid: e.g., diffusion, van-der-Waals forces, adhesion, particle-particle necks and electrostatic interactions. Commonly, semi-solid rheology is measured in terms of the apparent and / or complex viscosity η in experimental rheometers (either rotating bob or oscillating plate geometry). These measurements require a very sophisticated and costly setup since they have to cover some 8-10 orders of magnitude of viscosity. Systematic dependencies of η on temperature, hence on solid fraction, shear rate and time have been well studied [6]. These observations are however not visual and, hence, insufficient to fully describe and predict the die casting process. The quality of the latter can only be judged ex-situ from the cast components (e.g. spiral or other testing moulds), whereby the die filling properties of SSC are known to be rather poor for the casting of thin components. This drawback is not only due to the higher viscosity of the mixture as compared to the liquid, but also to demixing which is taking place during SSC. Thereby, the furthest extremities of the mould, particularly in thin geometries, fill mostly with liquid, while the solid fraction of the core is raised artificially. Consequently, microstructure and mechanical properties of the components become inhomogeneous. For binary or quasi-binary alloys this demixing can further lead to reduced fatigue strength because the liquid phase with its higher concentration of alloying elements has a more brittle microstructure. In order to learn more about this demixing of solid and liquid, the die filling process has to be observed in situ.

The authors have recently presented first results on an in situ visualization of semi-solid Al-Ge alloy injected through a thin cavity and recorded by synchrotron X-ray radioscopy [7]. Yet,

the employed acquisition rate of 66 images/s and below showed to be at least an order of magnitude too slow to follow the real injection process, whereas this rate was found to be well suited to study granular deformation mechanisms in semi-solid alloys under shear [8, 9, 10]. For this work, the previously described experiment could be extended to a rate of 500 images/s by moving to the high energy beamline ID15a of the European Synchrotron Radiation Facility (ESRF), Grenoble, France. ID15a has a photon flux density which is sufficient to record high-resolution radiographs at this high rate [11, 12]. Also the in situ setup has been developed further, in terms of temperature control and injection speed. For the present work we used two different thin channels to compare for the injection of an Al-Ge32 alloy: a) a bottleneck (similar to our previous study [7]), b) a right-angle turn channel. Optical flow analysis was then applied to track and to quantify particle and liquid motion in the measured data. This work demonstrates the unique capabilities of third generation synchrotron light sources to visualize microscopic deformation of semi-solid metals in situ.

2. Materials and methods

2.1. Semi-solid injection process

Figure 1 shows two photographs of the experimental setup which consists of an in situ furnace with a linear motor driving injection, and an imaging system. The furnace is an aluminium case fully covered with vermiculite plates in order to shield the heat which is produced by four Osram Xenophot 64635 HLX heating lamps (150 Watts, 15 Volts) which are slightly defocused and point towards the sample holder. The holder is a sandwich of two structured boron nitride (BN) plates which are held together by an alumina frame, as discussed in Zabler et al. 2010 [7]. A 0.5-mm thin thermocouple (Ni-Cr(+)/Ni-Al(-) type K, Thermocoax SAS, France) protrudes into the BN sandwich right next to the piston, just 1 mm to the right of the flow channel. The X-ray pencil beam enters and leaves through two holes in the front and back of the vermiculite plates and only passes through the BN structure. A 0.4-mm sheet of stainless steel (304 L) is attached to a linear stepping motor (Phytron, Inc., USA) and serves as a piston, driving downwards into the sandwich structure at 20 mm/s maximum velocity, thereby injecting the semi-solid material into the channel. The alloy Al-Ge32(wt.%) was chosen for being very similar to commercial Al-Si7 alloys concerning microstructure, yet having a larger X-ray density contrast between liquid and solid phase. The temperature for the SSC process is lower than in AlSi7, given by the solidus temperature of ~420°C and liquidus temperature of ~550°C). Small platelets of 7 mm x 3 mm x 0.4 mm were cut from as-cast ingots

to which 4 wt.% Al-Ti5-B grain refiner (Affilips Netherlands) were added to obtain a fine equiaxed microstructure. Prior to the experiments, all samples were heat-treated for 1 h in the semi-solid state at 480°C to produce coarse globular particles of about 50 µm average diameter.

Before starting the experiment, the effect of sample heating through irradiation by the X-ray beam was tested by placing a 4-mm thick piece of Al-Ge32 alloy in our setup with the lamps being turned off. The sample had a hole into which the thermocouple was placed and measured a temperature increase of 6 K while the X-rays were impinging onto the metal. Since the photon absorption of the 0.4-mm thick sample used for the radioscopy experiment was at least an order of magnitude smaller it is safe to assume that the heating by radiation was a few K at most. The two experiments, each with a different channel geometry, both took place at T = 520°C temperature. To exclude the possibility of a measurement error due to the thermocouple (shielded by an Al_2O_3 tube) which might be heated by the IR heating lamps or by scattered X-radiation, metallographic sections were recorded of the cold alloy microstructure after the radioscopy experiment. The velocity of the piston was set to 20 mm/s, the maximum acceleration being 80 mm/s^2. The amplitude of the movement was set to 8 mm, but the motion stopped earlier during both runs, i.e., when the solid skeleton had densified sufficiently through compression at the entrance of the BN-channel. After each experiment the samples were cooled down in air, extracted from the BN-sandwich and passed on for metallographic investigation under the light microscope.

2.2. Synchrotron-based microradioscopy

By employing hard polychromatic X-ray synchrotron radiation, radioscopy was successfully performed with acquisition rates ranging from a few hundred up to several ten thousand images per second [13, 14]. While X-ray inline phase contrast can frequently be employed in order to allow for high acquisition rates, our experiment required sufficient absorption contrast in order to separate qualitatively and quantitatively the liquid and the solid phase in the projection images. Hence, the high flux and high energy beamline ID15a (ESRF) was chosen to carry out this study: An outstanding high photon flux density is available, while the demands on coherence are less stringent. The employed insertion device of the beamline is an asymmetric multipole wiggler (1.84 T, 44 keV critical energy, further details available online [15]). ID15a was operated in a so-called ‘white beam mode’: the radiation from the source was filtered only by approximately 20 mm of silicon resulting in a photon flux density of approx. 10^{15} ph/mm/s. The X-ray image detector was an indirect system, designed and constructed by

the ESRF detector group [16]: A commercial tele-lens projects the luminescence image of a scintillator screen via a mirror (periscope geometry) onto the sensor of a CMOS camera. The mirror is used in order to prevent direct exposure of the camera electronics to the intense synchrotron radiation. As luminescence screen, a 100-µm thick YAG:Ce (Ce-doped $Y_3Al_5O_{12}$) single crystal was chosen. This material is known to resist the high heat load of the white beam from a synchrotron light source as well as for its fast response time[11]. In order to acquire images with high frame rates, a Photron SA1 camera was used, which is based on a CMOS sensor with 1024 × 1024 pixels, each 20 µm in size and a true dynamic range of 800:1 grey levels (10 bit, with a 12 bit digitalization). The camera can acquire up to 5400 images/s in full-frame mode. A memory of 32 GB on board allows for the intermediate storage of the images acquired and hence defines the maximal length of the recordable high-speed movie. Due to the optical magnification, the complete detector operates with an effective pixel sampling of 5.5 µm (hence, the spatial resolution is R > 11 µm, according to the Shannon theorem). For this study the acquisition rate was 500 images/s ('bottleneck' movies) and 1000 images/s ('right-angle turn' movies). As the readout time of the CMOS sensor is in the µs range, each picture corresponds to an exposure of 2 ms or 1 ms, respectively. The detector was positioned as close as possible to the sample (approximately 0.1 m distance) in order to reduce X-ray inline phase contrast effects.

2.3. Image processing and optical flow analysis

For the task of particle and liquid flow analysis we used automated optical flow techniques which are built to find correspondences between successive frames. This technique relies on the formulation of a variational problem, and determines a displacement field as its solution [17]. The original raw data comprises a number of difficulties, such as low signal to noise ratio, low contrast between particles and bubbles and temporally non-uniform brightness flickering. Such problems have occurred in other optical flow computations of X-ray microradioscopy [18]. Since optical flow methods are very demanding on image quality, it was crucial to augment the original radiographs quality prior to optical flow computations. An advanced pre-processing routine was therefore derived to improve the raw data and meanwhile preserve spatial and temporal details. The routine starts by applying a 3D Hybrid median filter [19] to eliminate the high contrast speckle noise. In order to equalize the non-uniform brightness variations, we then apply a spatial high-pass filter. This part of the process removes large-scale brightness patterns and retains local details. Finally, we used an anisotropic diffusion filtering

to eliminate the image noise and at the same time to enhance particle edges. The entire image pre-processing was performed with the freely available ImageJ software [20].

In order to compute reliable flow fields we employed an advanced optical flow model, which takes into account multiple image features and a priori motion information. For the construction of the model we assume constancy of image brightness and of spatial intensity gradients [21]. This combined assumption is more suitable for the motion estimation, if the image features are of low contrast. To provide robustness against noise, the data constancy assumptions were extended by a combined local-global approach [22]. For the motion constraint we chose a flow-driven smoothness approach [21]. The rather high image acquisition rate (500 images/s) resulted in a smooth gradual motion of the constituents, from which we can benefit by introducing an additional spatio-temporal smoothness constraint [21]: i.e., the final model takes into account motion between more than two successive frames. Furthermore, to separate the motion of the liquid front from the flow of adjacent particles, the smoothness is adapted to a spatial mask covering the air-liquid interface (cf. Fig. 2). In order to cope with a large range of flow velocities a coarse-to-fine computation strategy [21] has been incorporated. The result of the optical flow computation is a displacement vector for each image pixel. In order to visualize the latter we use a colour wheel, which indicates the direction by colour and the velocity by brightness.

3. Results

Figure 2 shows three versions of a radiographic image (frame #140) taken from the bottleneck sequence [Movie1 download]: (a) the normalized raw data, (b) data after filtering, masking and noise reduction and (c) the calculated colour-coded flow field. Noise reduction through filtering was essential to provide sufficient quality for the flow analysis. One can clearly distinguish between liquid and solid phase whereby the latter appears darker due to the lower X-ray density of aluminium compared to the Ge-rich liquid matrix. Air bubbles are difficult to distinguish from the Al particles. Compared to the latter, they descend at higher velocities and appear darker in the radiographs (arrow 1 in Fig. 2b). Two or three small clusters of solid particles detached from the bulk and moved through the channel following the liquid-air interface (arrow 2 in Fig. 2b). Their velocity signal overlaps with the signal of the liquid-air interface. This overlap depends on a 'smoothness constraint' of the optical flow analysis, which is a compromise between flow continuity and flow detail. One isolated particle appears not to move at all in this frame (arrow 3), whereas the expanding liquid forms a semi-circular crest of

constant velocity (as expected for a Newtonian fluid). The movement of the solid bulk in the upper part of the radiograph is slow and thus can hardly be observed in Fig. 2c (arrow 4).

For the same frame which is shown in Fig. 2 the quantitative flow amplitude (without direction) is calculated and shown in Fig. 3. The liquid is found to advance at a maximum speed of 3.1 mm/s, with the air bubbles descending at relatively high speed, up to 3.9 mm/s. The speed of the particle cluster at the lower liquid-air interface is 1.6 mm/s, and the average speed of the solid bulk in the upper part of Fig. 3 remains < 0.3 mm/s. A projected time evolution of these elements is shown in Fig. 4. Here, the average velocity was projected for each pixel over several hundred frames, i.e. integrating from frame #50 to frame #250, while removing the velocities of the liquid front with a 3D contour mask [Movie2 download]. The resulting colour-coded velocity projection (Fig. 4a) shows solid particles, clusters and air bubbles. The latter follow a curved trajectory until the downwards directed pressure is balanced by the buoyant force and their motion describes a hook. The few particles, whose velocities overlap with the crest of the liquid front (cf. Fig. 2), are seen in the lower right. Quantitative velocity amplitudes are shown in Fig. 4b, which allow to draw velocity-path profiles (along the curved arrows), for air bubbles (path 1), and for particle clusters (path 2). The profiles are shown in Fig. 5 where the velocities of the air bubbles appear significantly faster (slightly slower than the liquid) compared to the particle cluster: 3 – 4 mm/s (before the bubble slows down and its velocity approaches 1 mm/s), compared to 0.5 – 1.0 mm/s for the cluster, respectively.

To investigate the flow of the solid skeleton over the remaining time sequence, average velocities were integrated from frame #250 to #450. The radiographs were again 3D-masked to separate liquid and solid. Figure 6 shows the average velocities for both components. Velocity of the solid particles appears to be of homogeneous amplitude, yet differing in direction, resulting in a faceted structure (cf. Fig. 6a). The integrated velocities in Fig. 6a also match with the silhouette of the final state of the solid skeleton reaching into the recipient (which was not fully filled by solid) and matches metallographic post-observations. On the other hand, the projected liquid flow appears smooth and homogeneously distributed, filling the entire cavity (cf. Fig. 6b). As expected from Bernoulli's law on fluids, the liquid velocity in the recipient (3 mm x 0.4 mm) equals 1/3 of the value which is measured in the narrower bottleneck (1 mm x 0.4 mm).

Figure 7a shows the last radiography of the sequence, Fig. 7b the corresponding metallographic section which was prepared after the experiment. The microstructure shows

portions of the alloy which were fully liquid at the end of the experiment and hence secondary Al-dendrites formed during cooling. The volume fraction of these dendrites is calculated from the metallographic sections and marks a fixed point on the liquidus line in the binary phase diagram, hence the temperature during the experiment. The 35-40 vol.% which are found are in good agreement with the measured 520 ˚C which corresponds to a value of 38 vol. % for the secondary dendrites. Hence, the solid fraction at 520 ˚C is 22 vol.% according to the binary phase diagram.

When the experiment is carried out with a different channel geometry (right-angle turn) the flow behaviour is expected to change [Movie3 download]. The right-angle was chosen to create a more turbulent flow, in the hope that the motion of both liquid and solid would be more conjoint compared to the bottleneck. Figure 8 shows a series of three radiographs situated in the middle of the sequence (a-c) covering about 0.2 s, and the metallographic section of the final structure (d). The solid phase appears indeed to stay closer to the liquid front, larger round air bubbles move along and disappear at some point of time. Projection maps of average velocity (directional, i.e. colour-coded) of the solid phase are shown in Fig. 9 for the right-angle geometry, along with an attempt to divide the channel into three distinct regions: I, II and III. Fig. 9 results from integration over the first half of the sequence, hence frame #100 to #450. The colour-coding clearly shows that in region I the solid phase moves in curved trajectories through the channel following the right-angle turn (cf. Fig. 9a). Yet, in the lower part of the channel (region II) hardly any movement takes place. The motion in region III is directed downwards and reveals slow particle motion as well as some larger bubbles descending faster (cf. Fig. 9b). Numerous particles which exhibit momentarily some turbulent motion appear as bright coloured speckles. Some of these speckles correspond to air bubbles like the ones observed in Fig. 4a, but some are actually particles whose velocities remind of a Brownian-like motion. An example for this motion can be seen in Fig. 10. During a series of 23 frames the particle appears to detach from a large cluster and moves in various directions before re-joining the solid skeleton. An example of spontaneous break-up of a larger particle cluster from the latter is displayed in Fig. 11. A large region of the solid, approx. 1.5 mm in diameter which is located at the interface between region I and II, remains frozen for approx. 35 ms (Fig. 11a), then suddenly the upper half of this cluster moves at high speed into separate directions, indicated by several flares in Fig. 11c (velocity amplitude), while the lower part remains still.

4. Discussion

Compared to our previous experiments [7] the present data shows a multitude of dynamic effects, particularly for the new geometry (right angle turn) of the flow channel. Here, isolated turbulent particle motion and transition from a frozen solid skeleton to moving particle / clusters could be observed. The latter, we believe, is the first visual proof of the thixotropic break-up during semi-solid injection. Concerning the bottleneck channel our results match previous observations of slower injections [7], despite being an order of magnitude faster than the latter. When the channel narrows, only few particles traverse the bottleneck, the remains accumulate at the entrance. The solid movement comes to a complete halt, when the liquid has fully filled the recipient, balancing the top-down pressure from the piston or when the compressed solid particles block further flow through the channel. Compared to the slower experiments, we used a higher temperature and hence a smaller solid fraction (22 vol% instead of 48 vol%), as well as a faster piston (20 mm/s instead of 2 mm/s). The transport of particle clusters through the bottleneck appears to be hindered mainly by inter-particulate friction (with the exception of a few particle clusters moving directly on the crest of the liquid-air interface). This can be explained by the particle clusters moving independently, often not along a straight line and with possible rotations and mutual collisions. Our results show clearly the inter-particulate as well as the particle-wall friction to be the hindering force during semi-solid injections through thin cavities.

Concerning the data interpretation we have adapted algorithms by means of optical flow analysis for the tracking of in situ rheological motion of semi-solid melt by introducing and adjusting a variety of numerical constrains (such as smoothness, flow-driven approach) based on different assumptions (e.g. constancy of total brightness and of gradients). Compared to the raw data which was prone to brightness artefacts and strong image noise, the resulting flow charts are impressively clear. Our computation is not limited to the present problem, many other applications exist: e.g., motion of granular material and high-speed X-ray movies of laser welding, where ceramic particles serve as contrast agent to visualize the flow of the melt. Our experiments are the first to visualize semi-solid metal flow at such high speed (500 images/s and 1000 images/s, i.e. 2 ms and 1ms sampling of the time domain, respectively). By applying optical flow analysis, velocities up to 5 mm/s were measured for the liquid, 3.6 mm/s for the solid phase. Note, that the piston which accelerated downwards, reaching 20 mm/s maximum speed was much faster than the liquid. Yet, the latter was also sucked up through the gap

between BN walls and the downwards driving piston, thus reducing the pressure, which explains the somewhat low velocities measured with this experimental setup. Recording even faster scenes on the same beamline (ID15a) is unlikely to provide more details, since the signal-to-noise ratio (SNR) of the present movies shows the very limit required by the flow analysis. On the other hand, using the polychromatic spectrum of a beamline with softer X-emission (e.g. 20-50 keV) could raise the absorption contrast (which in this study was μt = 0.45, with μ being the attenuation coefficient and t the effective thickness of the sample along the X-ray beam path) and thus the SNR. Recently, on the ID19, radioscopic movies of metal foaming were recorded at a rate as high as 105 000 images/s using a wiggler source in 'white-beam mode' [23, 24].

5. Conclusions

The comparison of the semi-solid flow through two types of thin channel geometries indicates a significant influence of the latter on the filling properties of semi-solid metals. During injection into the bottleneck channel, only little solid material could descend through the channel into the cavity, which was hence mainly filled with liquid. On the contrary, both solid and liquid phase moved relatively conjointly through the right-angle turn in the second experiment, which was found to locally exhibit turbulent flow resulting in Brownian-like particle motion and breakup of larger clusters into smaller particles. Events showing the appearance and disappearance of gas bubbles were more frequently observed in the right-angle turn. It appears that the less laminar flow of the liquid which takes place in such channel-turns and -corners allows the solid skeleton to advance at a similar speed with the liquid. The problem of the bottleneck is that the slow network of solid particles at the top entry into the channel is all too quickly depleted from liquid phase which is needed by the particles to move. Since the overall amount of liquid is limited by the composition of the alloy, it is only at the very beginning of the experiment that solid particles are crossing the channel. An interesting variation of this experiment would be to put a larger piece of Al-Ge alloy (with a Ge-concentration high enough to fully melt the piece) on top of the semi-solid Al-Ge32, thus providing a continuous flow of liquid during the injection. One unexpected conclusion of this study is that during the semi-solid injection, the diffusion and dissolution of the constituting elements is slow compared to the motion of solid and liquid phase. One could therefore easily use more liquid without dissolving the solid phase.

The next logical step would be to vary the temperature during the experiment thus

changing the solid volume fraction of the mixture. Yet, the present results show that already a fraction as low as 22% has problems penetrating the bottleneck. Another step ahead would be to compare the radioscopic observation with 3D finite element studies of the semi-solid flow. The impact of particle size and shape could thus be tested.

Acknowledgements

We would like to thank the ESRF for generously granting the beamtime (MA 485). Matthew Peele provided excellent support as 'local contact' on ID15A. Further thanks go to Lukas Helfen and Tomy dos Santos Rolo and David Haas who participated in the campaign. The project was supported through the European space agency's grant no. ESA-MAP AO-99-075.

References

[1] Flemings MC, Metall. Trans. A 1991, 22:957-81.

[2] Spencer DB, Mehrabian R, Flemings MC, Metall. Trans. B 1972,3:1925-32.

[3] Fan Z, Int. Mater. Rev. 2002, 47:49-85.

[4] Laxmanan V, Flemings MC, Metall. Trans. A 1980,11:1927-37.

[5] Perez M, Barbe J-C, Neda Z, Brechet Y, Salvo L, Acta Mater 2000,48:3773-82.

[6] Hufschmidt M, Modigell M, Petera J, J Non-Newtonian Fluid Mech 2006, 134:16-26.

[7] Zabler S, Rack A, Rueda A, Helfen L, Garcia-Moreno F, Banhart J, Phys Stat Solid A 2010,207(3):718-23.

[8] Nagira T, Gourlay CM, Sugiyama A, Uesugi M, Kanzawa Y, Yoshiya M, Uesugi K, Umetani K, Yasuda H, Scripta Mater 2011, 64(12):1129-32.

[9] Gourlay CM, Dahle AK, Nagira T, Nakatsuka N, Nogita K, Uesugi K, Yasuda H, Acta Mater. 2011, 59(12):4933-43.

[10] Zabler S, Rueda A, Rack A, Riesemeier H, Zaslansky P, Manke I, Garcia-Moreno F, Banhart J, Acta Mater. 2007, 55:5045–55.

[11] Di Michiel M, Merino JM, Fernandez-Carreiras D, Buslaps T, Honkimäki V, Falus P, Martins T, Svensson O, Rev. Sci. Instrum. 2005, 76:043702.

[12] Rack A, Garcia-Moreno F, Schmitt C, Betz O, Cecilia A, Ershov A, Rack T, Banhart J, Zabler S, J. X-Ray Sci. Techn. 2010, 18(4):429-441.

[13] Garcia-Moreno F, Rack A, Helfen L, Baumbach T, Zabler S, Babcsan N, Banhart J, Martin T, Ponchut C, Di Michiel M, Appl. Phys. Lett. 2008, 92(13):134104.

[14] Rack A, Garcia-Moreno F, Baumbach T, Banhart J, J. Synchrotron Rad. 2009, 16(3):432-4.

[15] ID15 High Energy Diffraction and Scattering Beamline. http://www.esrf.eu/UsersAndScience/Experiments/StructMaterials/ID15 (2011).

[16] Koch A, Nucl. Instrum. & Meth. Phys. Res. A 1994,348:654–8.

[17] Horn B, Schunck B, Artificial Intelligence 1981, 17:185–203.

[18] A. Myagotin, A. Ershov, L. Helfen, R. Verdejo, A. Belyaev and T. Baumbach, J. Synchrotron Rad. 2012, 19.

[19] 3D Hybrid Median Filter Plugion for ImageJ http://rsbweb.nih.gov/ij/plugins/hybrid3dmedian.html

[20] W.S. Rasband, ImageJ, U.S. National Institutes of Health, Bethesda, Maryland, USA, http://imagej.nih.gov/ij/, 1997-2011.

[21] Brox T, Bruhn A, Papenberg N, Weickert J, in T. Pajdla, J. Matas (Eds.): Computer Vision – ECCV 2004, Lecture Notes in Computer Science, Springer 2004, 3024:25–36.

[22] Weickert J, Schnörr C, J Math Imag & Vis 2001, 14(3):245–55.

[23] Rack A, Garcia-Moreno F, Helfen L et al., Appl. Opt. 2012, in preparation.

[24] Garcia-Moreno F, Mukherjee M, Jimenez C, Rack A, Banhart J, Metals 2012, 2(1):10-21.

Figure Captions

Fig. 1: (a) Experimental hutch of the ID 15A high energy beamline at the European Synchrotron Radiation Facility (ESRF) with the in-situ furnace and detector used for the present study. (b) Close-up view into the open in-situ furnace: The BN sandwich plates with the channel structure (inset) is clamped by an Alumina frame which is placed in the middle of four Xenophot heating lamps; a linear stepping motor drives down the piston (a thin sheet of stainless steel) into the sandwich structure thus injecting the semi-solid mixture during the in-situ experiment.

Fig. 2: Three versions of radiograph #140 from the 'bottleneck sequence'. (a) Normalized raw data ($-\log(I/I_0)$) showing liquid and solid phase during the injection, the latter appearing less bright due to its lower density. (b) Masked and filtered raw data: Only the semi-solid mixture is seen, not the recipient, noise is reduced for the optical flow analysis. (c) Calculated flow map (color encodes direction, brightness equals speed) according to the color wheel at the bottom right. Arrows: (1) air bubbles, (2) cluster of particles moving at high speed on the crest of the liquid front, (3) particle which is not moving at all according to optical flow analysis, (4) slowly moving bulk skeleton. The

grey silhouette represents the mask which was applied during flow analysis.

Fig. 3: Quantitative motion amplitude of the optical flow in frame #140. Brightness shows the quantitative velocity given in units of mm/s.

Fig. 4: Projected average velocity, integrated from frame #50 to frame #250: (a) color-coded motion showing the curved trajectories of air bubbles as well as several solid particle clusters which can be seen at the lower right. (b) Quantitative motion amplitude (scale bar in units of mm/s) with two arrows indicating the curvilinear path along which velocity-versus-path profiles were calculated. The grey silhouette marks the perimeter of the liquid phase in the current frame.

Fig. 5: Two velocity profiles extracted from the quantitative maximum velocity map in Fig. 4b. The motion of the air bubble is shown by the dashed line, whereas the slower movement of a particle cluster is shown as a straight line. Units have been converted to mm/s and mm.

Fig. 6: Projected average velocities, integrated over several hundred frames (a) frame #250 to frame #450: color-coded motion of the solid phase, and (b) frame #50 to frame #450: Liquid phase. The grey silhouette in indicates the masking during the optical flow analysis (b) and the final perimeter of the liquid (a).

Fig. 7: (a) Frame #500 of the bottleneck sequence and (b) the corresponding metallographic section which was prepared and photographed under the optical microscope after the in-situ experiment. Note, the part of the metal which is liquid in (a) appears to be filled with secondary Al-dendrites in (b). The volume fraction (35-40 %) of the latter was used to estimate the temperature during the experiment.

Fig. 8 Sequence showing frames #250, #350 and #450 of the 'right-angle turn sequence' as well as the metallographic section which was prepared after the experiment. From (a) to (c), 0.2 seconds passed between each picture. The channel width is 3 mm, its depth 0.4 mm.

Fig. 9: Projected average velocities, integrated over frames #100 to #450 during injection through the right-angle turn: (a) color-coded motion of the solid phase indicated that different flow regions are present, which are illustrated in (b) I: laminar sideways flow, II: static region, and III: slow vertical flow.

Fig 10: a) Example of turbulent motion in the right angle turn channel. b) Magnified region of interest. (c-f) Color-coded turbulent motion of a single particle recorded over 23 frames. The arrows indicate the direction of particle motion as well as the velocity amplitude (length).

Fig. 11: Example of spontaneous breakup of a larger cluster of particles. Pictures show radiographs of the right angle turn with the super-imposed velocity amplitude as brightness: a) Frame #270, rectangle indicates a region where only little motion of the solid phase is observed. b) In frame #296 the solid skeleton in the same region has come to a complete halt. c) 34 frames later (#330) the static structure breaks up into many parts.

Fig. 1

Click here to download high resolution image

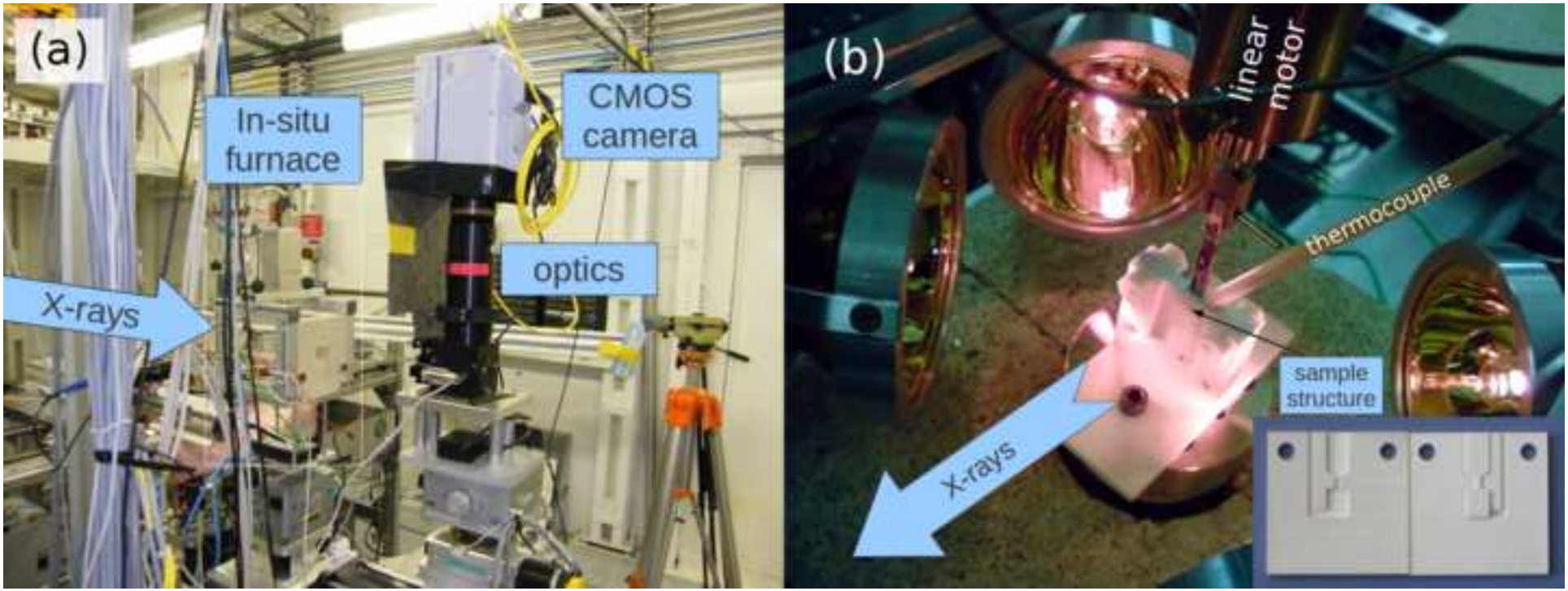

Fig. 2

Click here to download high resolution image

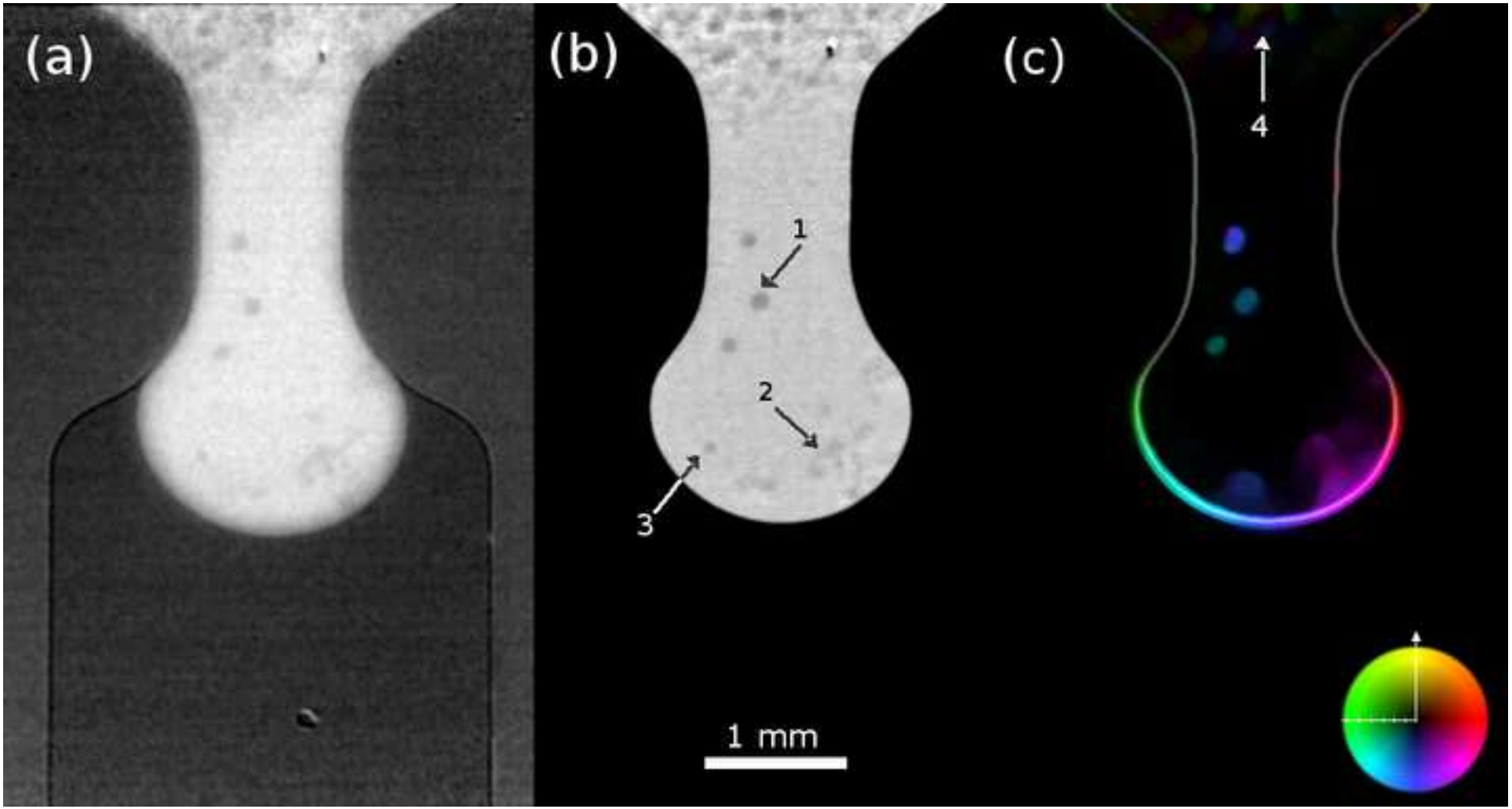

Fig. 3

Click here to download high resolution image

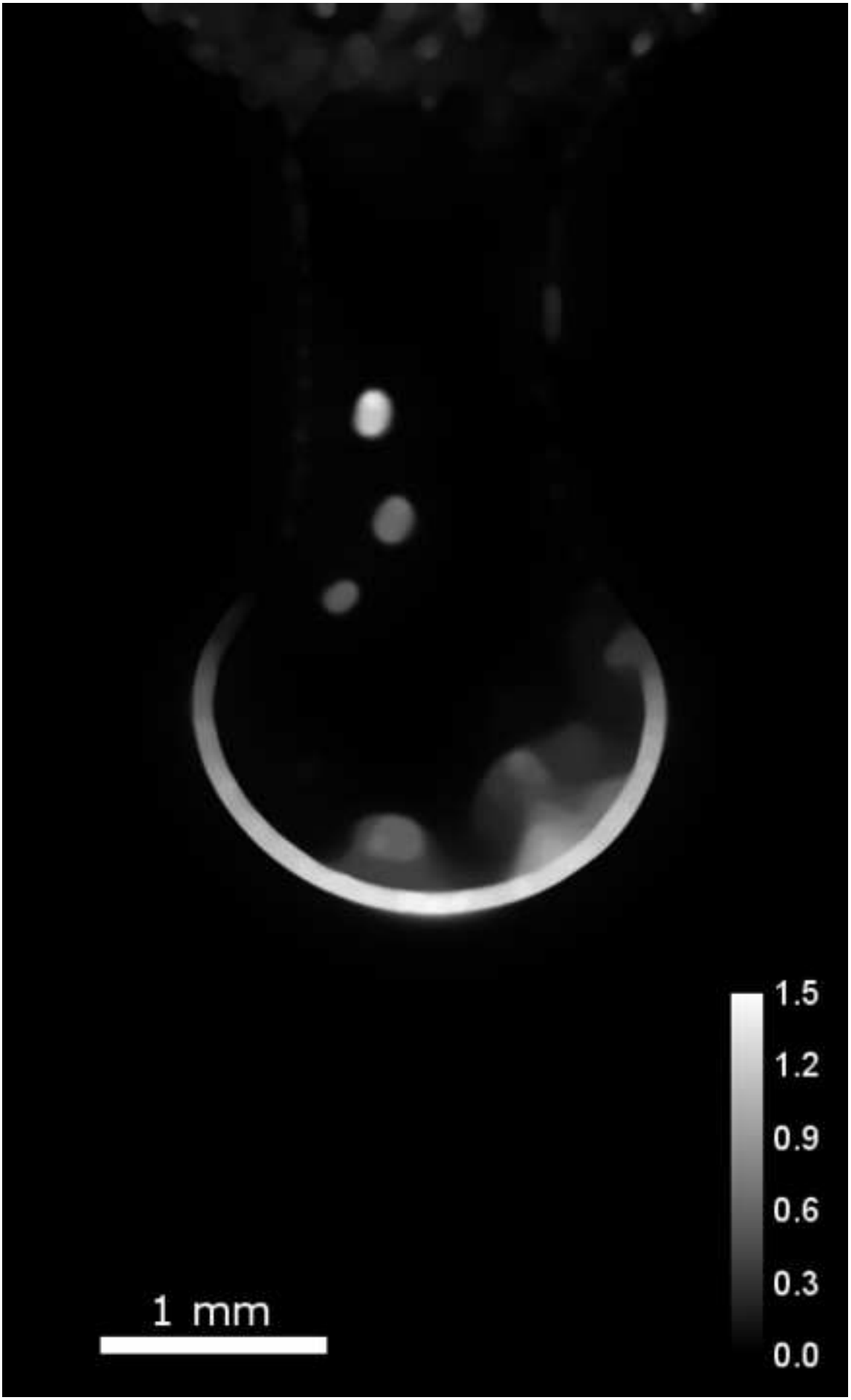

Fig. 4

Click here to download high resolution image

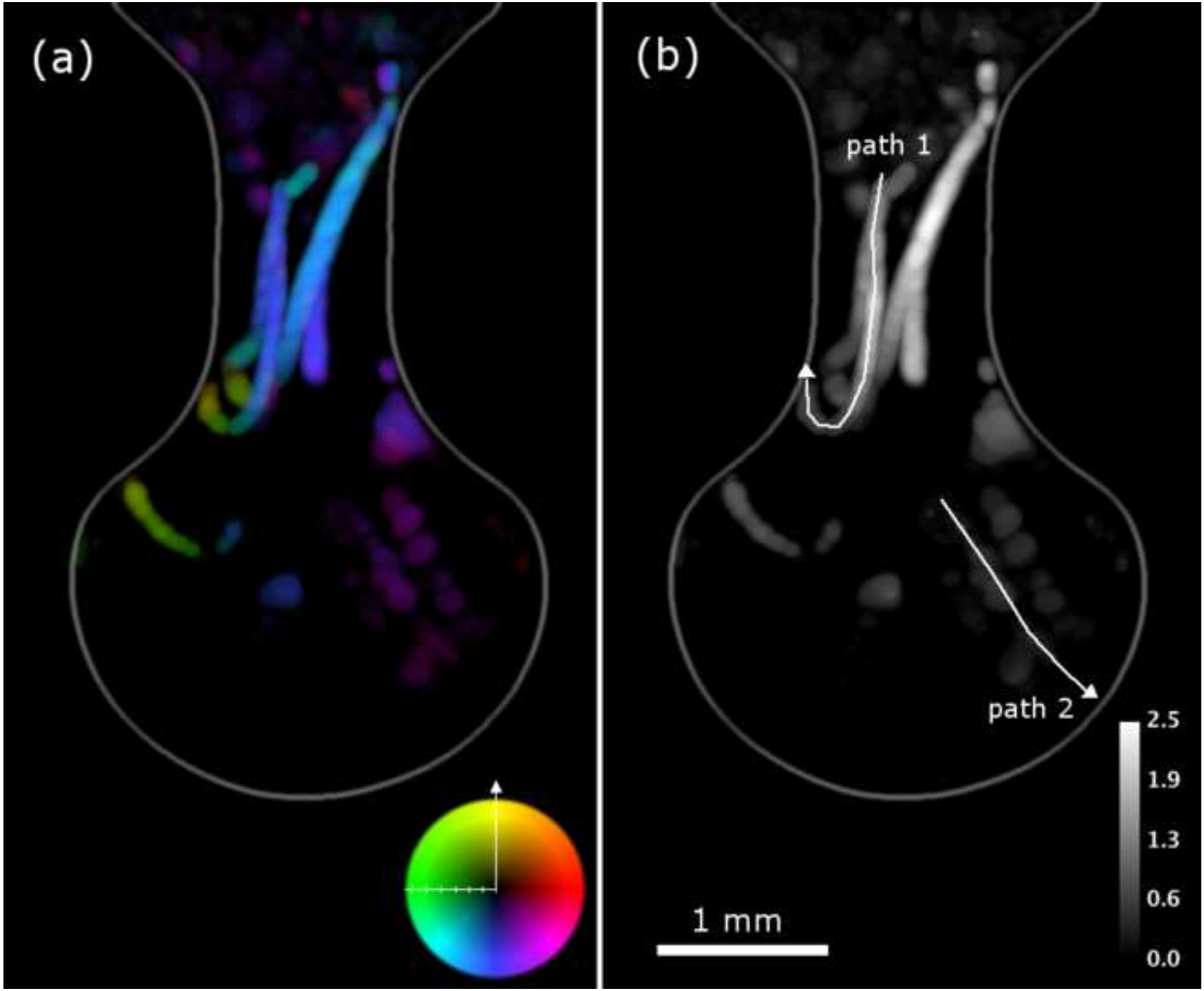

Fig. 5

Click here to download high resolution image

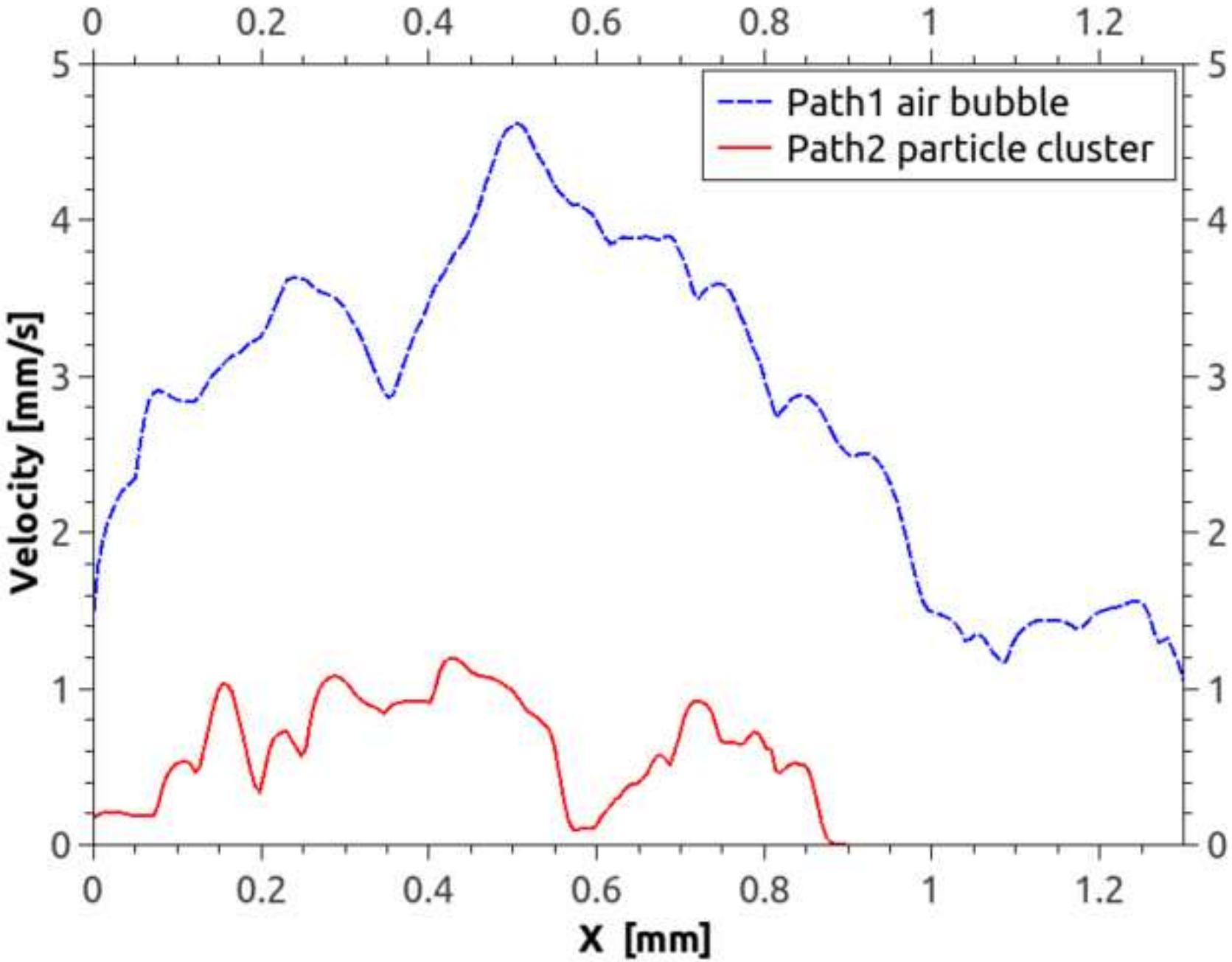

Fig. 6

Click here to download high resolution image

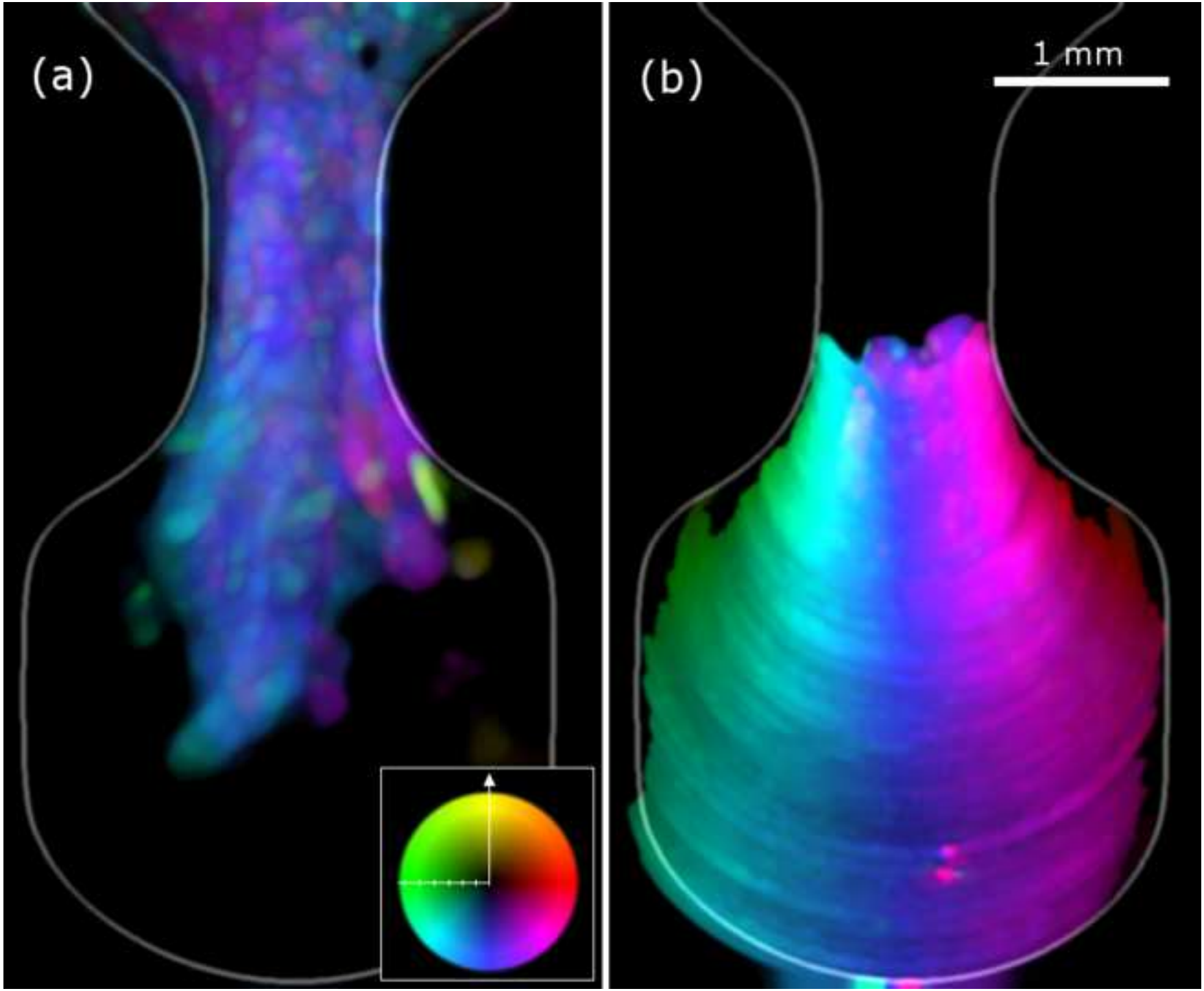

Fig. 7

Click here to download high resolution image

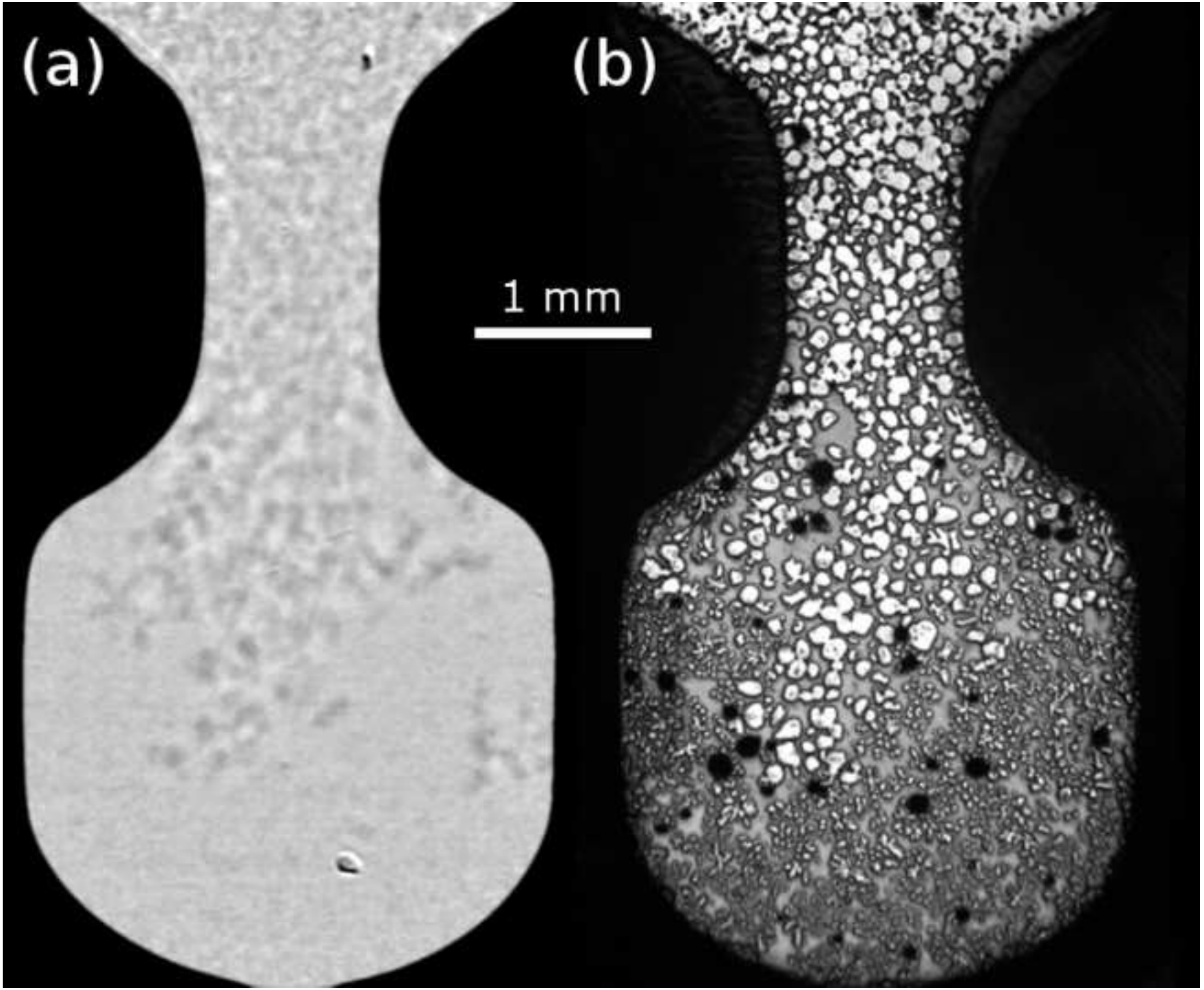

Fig. 8

Click here to download high resolution image

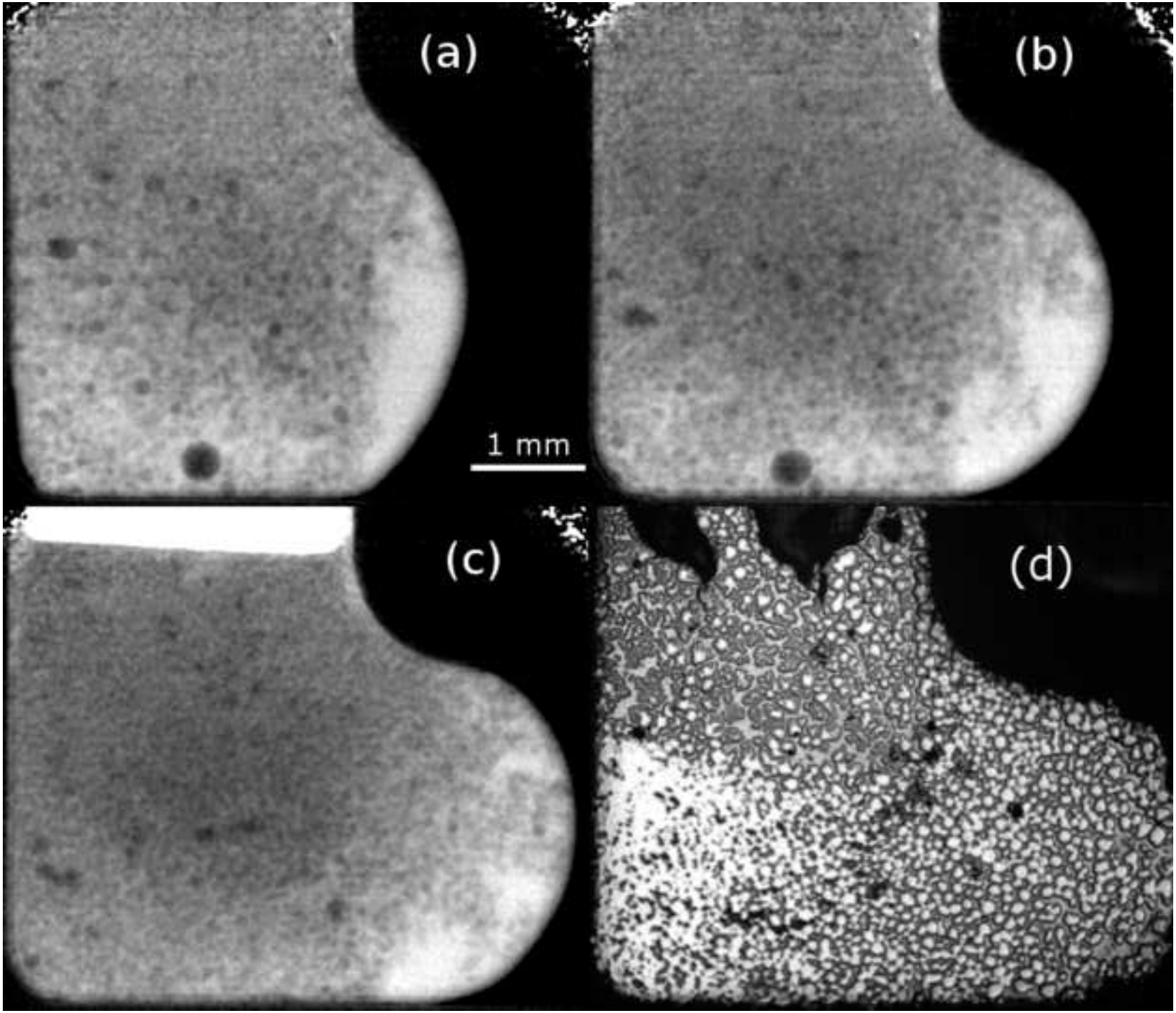

Fig. 9

Click here to download high resolution image

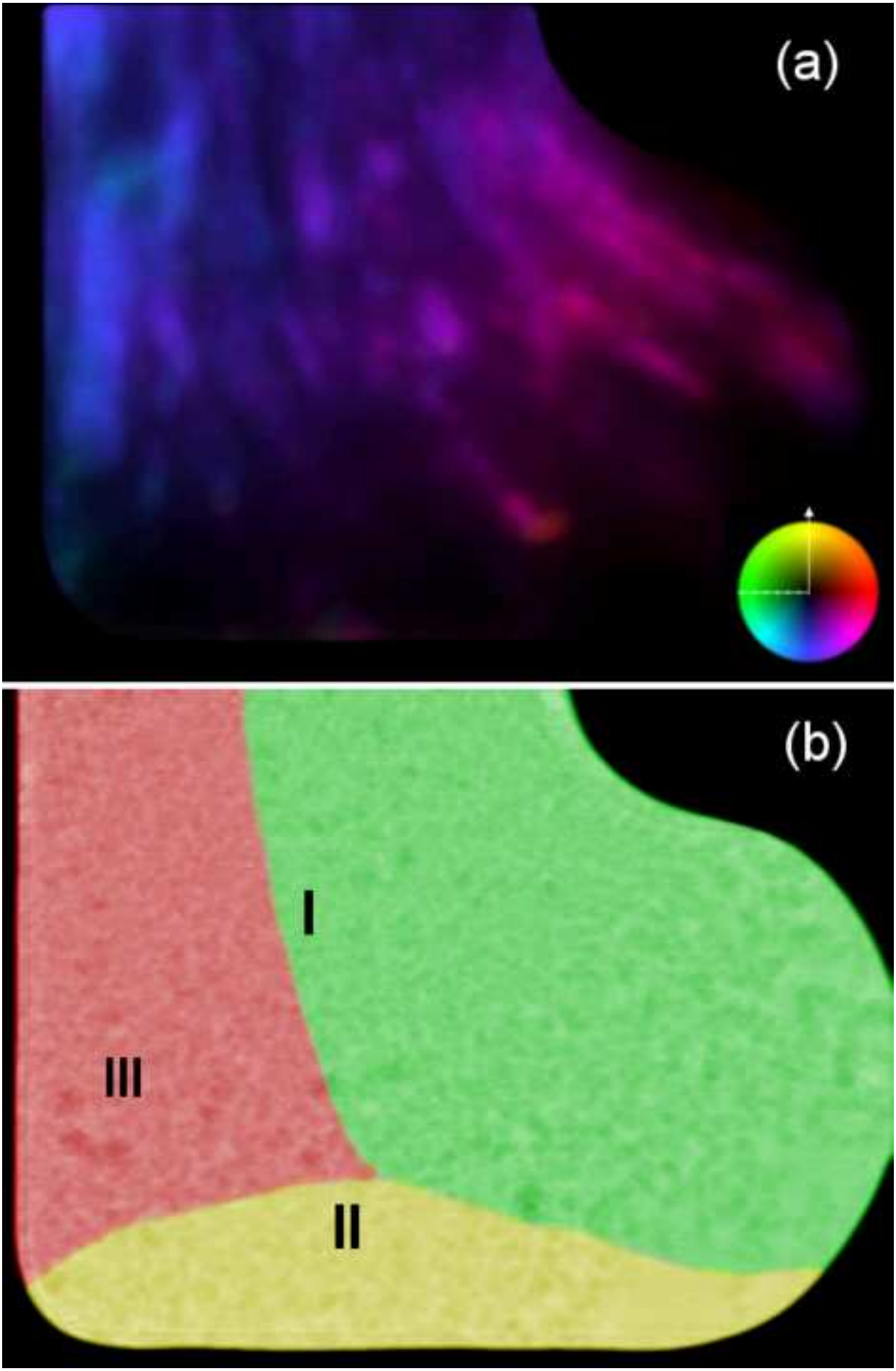

Fig. 10

Click here to download high resolution image

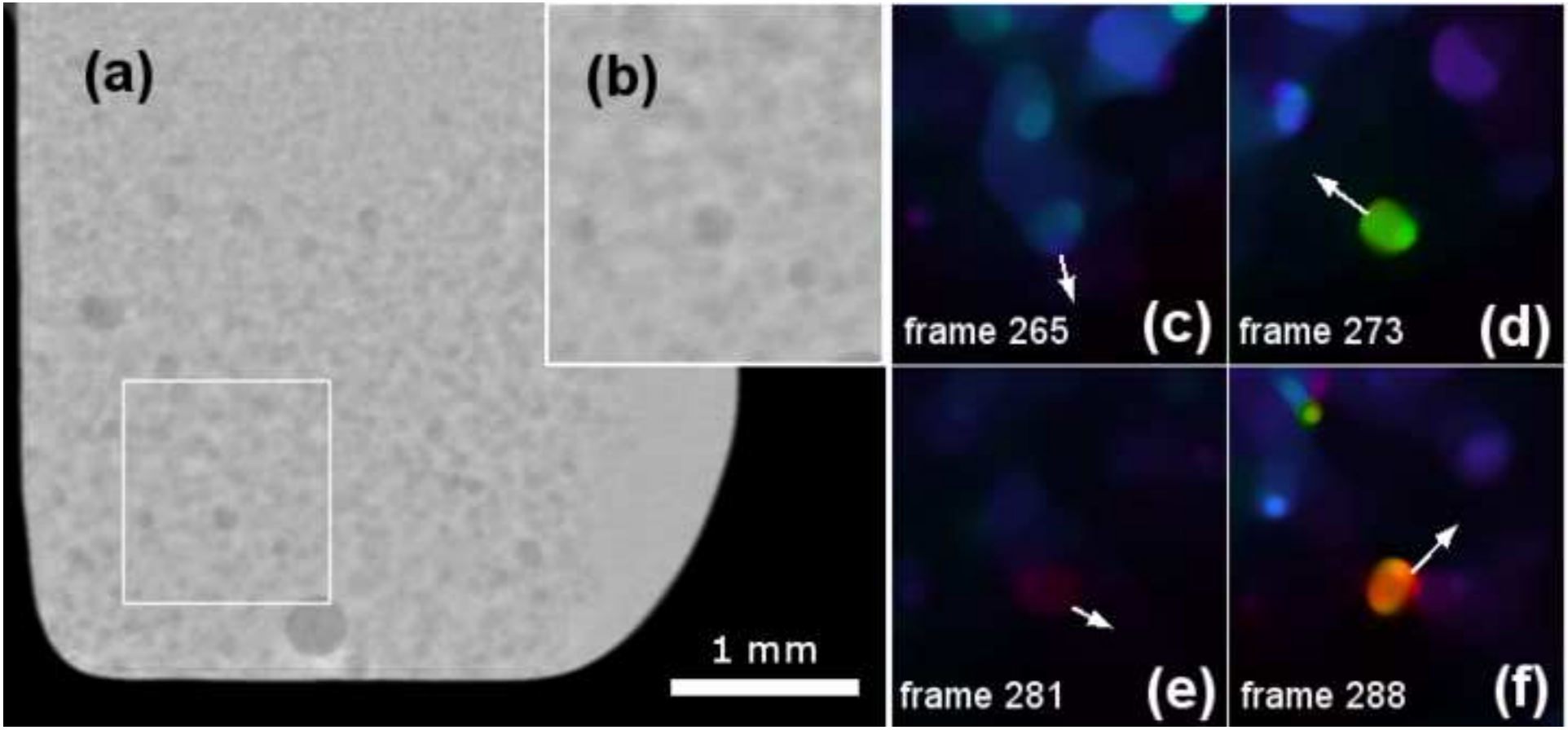

Fig. 11

Click here to download high resolution image

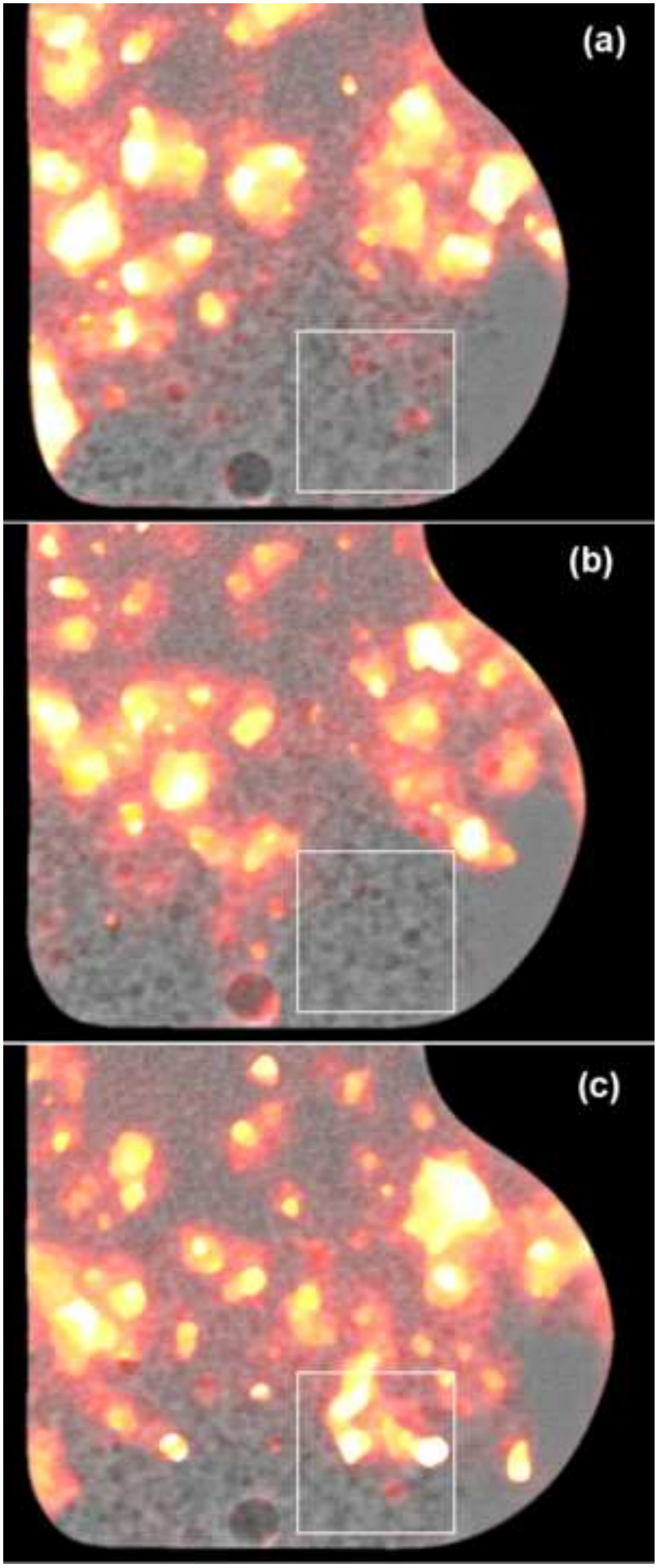

Movie 1

Click here to download Supplementary Material: movie1_flow_field_mpeg4.mp4

Movie 2

Click here to download Supplementary Material: movie2_flow_trajectories_mpeg4.mp4

Movie 3

Click here to download Supplementary Material: movie3_flow_vectors_mpeg4.mp4

Video Still 1

Click here to download high resolution image

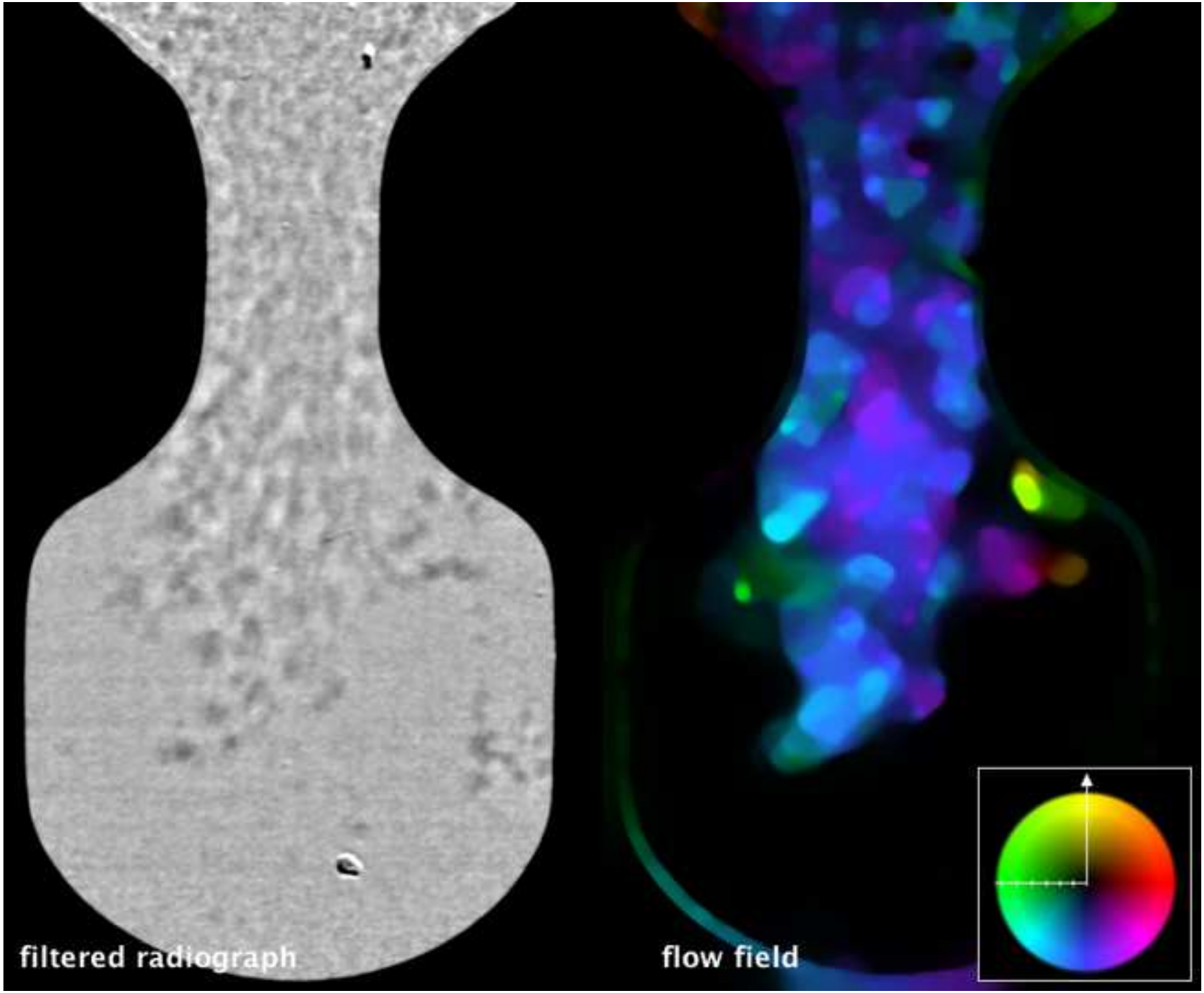

Video Still 2

Click here to download high resolution image

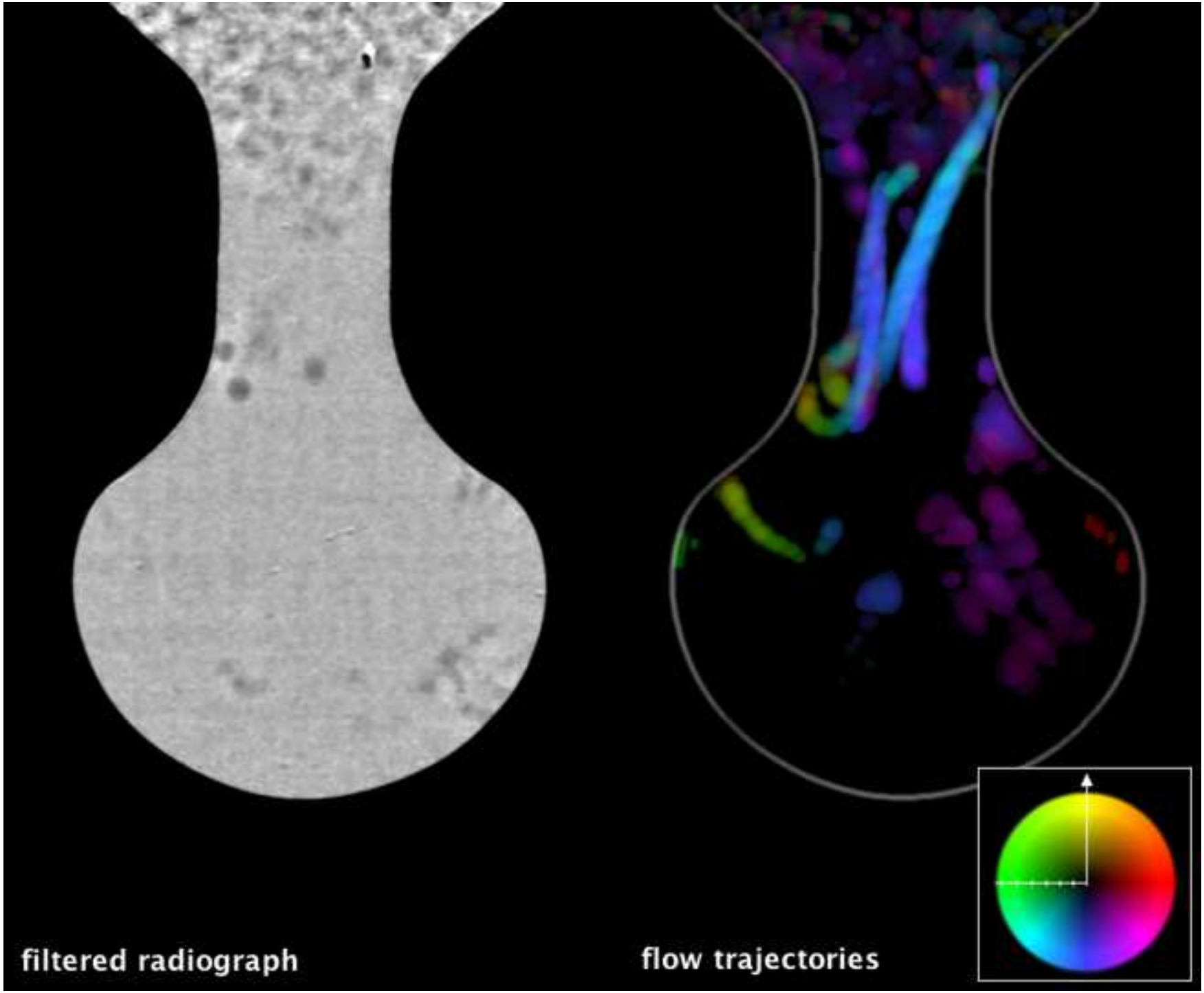

Video Still 3

Click here to download high resolution image